Valley spin-acoustic resonance in MoS_2 monolayers

K. Sonowal,[1,2] D. V. Boev,[3] A. V. Kalameitsev,[3] V. M. Kovalev,[3,4,*] and I. G. Savenko[1,2]
[1]*Center for Theoretical Physics of Complex Systems, Institute for Basic Science (IBS), Daejeon 34126, Korea*
[2]*Basic Science Program, Korea University of Science and Technology (UST), Daejeon 34113, Korea*
[3]*Rzhanov Institute of Semiconductor Physics, Siberian Branch of Russian Academy of Sciences, Novosibirsk 630090, Russia*
[4]*Novosibirsk State Technical University, Novosibirsk 630073, Russia*

(Received 22 June 2022; revised 16 September 2022; accepted 27 September 2022; published 26 October 2022)

The band structure of a monolayer MoS_2 comprises spin-split subbands, owing to the mutual presence of broken inversion symmetry and strong spin-orbit coupling. In the conduction band, spin-valley coupled subbands cross each other at finite momenta, and they are valley degenerate. When exposed to surface acoustic waves, the emerging strain-induced effective magnetic fields can give rise to spin-flip transitions between the spin-split subbands in the vicinity of the subband crossing point, resulting in the emergence of a spin-acoustic resonance and the acoustoelectric current. Resonance peaks occur at acoustic frequencies of gigahertz range in the vicinity of the subband crossing point. An external magnetic field breaks the valley degeneracy, resulting in the valley-selective splitting of spin-acoustic resonances, both in surface acoustic wave absorption and acoustoelectric current.

DOI: 10.1103/PhysRevB.106.155426

I. INTRODUCTION

Monolayer transition-metal dichalcogenides (TMDs) [1,2] represent direct-band-gap semiconductors with a hexagonal lattice possessing two inequivalent valleys related to each other by time-reversal symmetry. They are at the center stage of recent developments in condensed-matter physics, as they demonstrate a variety of fascinating physical phenomena [3–12]. One such phenomenon in monolayer TMDs is the spin-valley coupling [13] arising due to the coexistence of inversion symmetry breaking and strong spin-orbit coupling (SOC). As a result of spin-valley coupling, a spin splitting occurs, resulting in a unique band structure with the conduction and valence bands split into spin-polarized subbands with opposite spin orientation in both the valleys.

The band structures of different TMDs have been studied lately in detail using the tight-binding model and such methods as the $\mathbf{k}\cdot\mathbf{p}$ and density functional theory [2,14–17]. In particular, the findings reveal different nature of spin splittings in molybdenum-based compounds (MoX_2) and tungsten-based compounds (WX_2). The dispersion of spin-split electron states in MoX_2 possesses specific features. In particular, the spin-up and spin-down branches cross at finite value of the electron momentum, while no such crossings happen in WX_2. For the particular case of MoS_2, an effective splitting of spin-resolved branches varies from 3 meV at small electron momenta to zero at the electron momenta corresponding to the crossing of spin-split branches.

This property potentially allows for the emergence of electron spin-acoustic resonance (SAR) phenomenon [18] in MoS_2, which is the subject of this paper. SAR involves the selective absorption of energy by the two-dimensional (2D) electron gas from the acoustic vibrations corresponding to energies equal to the difference between the spin-split subbands, resulting in resonant transitions between the subbands due to spin-phonon interactions. We calculate the transition probability of spin-flip processes induced by surface acoustic waves (SAWs) in semiconducting structure consisting of a MoS_2 monolayer located on the semi-infinite substrate surface on which the Rayleigh SAWs travel. Initially discovered in paramagnetic materials [19–24], later SAR was also studied in silicon carbide and nitrogen vacancy centers in diamond [18,25–28] by exposing them to SAWs. They represent a powerful tool to study a variety of transport phenomena [29–32].

SAWs have been used to manipulate electrons not only in TMDs [33,34] but also in other 2D materials, such as graphene [35–38] and black phosphorus [39,40]. In our previous works [4,5], we studied acoustoelectric effect in TMDs, disregarding the effects of spin-orbit coupling. Here, the interaction of spin-polarized conduction-band electrons in spin-split subbands with SAWs is the focus of research. The main effect discussed here is the spin-acoustic resonance that is specific to monolayer MoS_2 due to its unique band structure, unlike the acoustoelectric effect [4,5], which can be observed in different TMD materials. We also study the acoustoelectric current here, which arises in the system as a consequence of transfer of SAW momentum to the electron subsystem accompanied by the spin-flip transition processes.

Furthermore, an external magnetic field breaking the time-reversal symmetry [41,42] results in an additional Zeeman splitting of the originally degenerate bands and thus, it allows for an additional control of the phenomenon in question. Indeed, the Zeeman splitting is opposite in different valleys, thus breaking the valley degeneracy of the entire

*Corresponding author: kavyashrees06@gmail.com

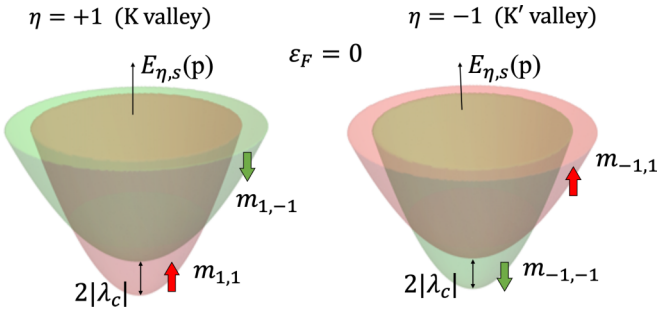

FIG. 1. Energy dispersions for valleys $\eta = \pm 1$ and spins $s = \pm 1$ plotted using Eq. (6), where the energy is shifted by $\Delta/2$.

system, which is reflected in the transition probability and the acoustoelectric (AE) current. Transport phenomena dependent on the combined effect of valley and spin degree of freedom in TMDs hold a promising future in various applications [43,44]. Acoustic resonances hold crucial significance in the development of quantum technologies and devices [25,29]. Its dependence on valley degrees of freedom can bring a huge enhancement and broadening of the potential of its present applicability.

II. DISPERSION OF SPIN-SPLIT SUBBANDS IN THE CONDUCTION BAND OF MoS_2 MONOLAYER

Up to the first order in electron momentum $\mathbf{p}$, the effective $\mathbf{k}\cdot\mathbf{p}$ Hamiltonian for the two-band model in MoS_2 reads [13,15]

$$H_0 = v(\eta p_x\sigma_x + p_y\sigma_y) + \frac{\Delta}{2}\sigma_z, \tag{1}$$

where v is the Fermi velocity, σ_i are the Pauli matrices, Δ is the gap between the conduction and the valence bands, and $\eta = \pm 1$ is the valley index. The intrinsic SOC term describing the spin splitting of valence and conduction bands reads as [45]

$$H_{SO} = \frac{\lambda_c\eta}{2}(\sigma_z + \mathcal{I})s_z - \frac{\lambda_v\eta}{2}(\sigma_z - \mathcal{I})s_z, \tag{2}$$

where $\mathcal{I}$ is the identity matrix in the pseudospin sector, λ_c and λ_v are the spin-orbit splittings of the conduction and the valence bands, respectively, and s_z is the spin Pauli matrix with eigenvalues $s = \pm 1$. Thus the total Hamiltonian reads $H = H_0 + H_{SO}$. The eigenenergies of this Hamiltonian corresponding to the spin-split branches of the conduction band are given by (Fig. 1)

$$E_{\eta,s}(\mathbf{p}) = \eta s\frac{\lambda_v + \lambda_c}{2} + \sqrt{\left[\tfrac{\Delta - \eta s(\lambda_v - \lambda_c)}{2}\right]^2 + v^2p^2}, \tag{3}$$

and the corresponding eigenstates of the electrons in the conduction band are

$$\Psi_{s\eta}(\mathbf{r}) = \begin{pmatrix} \cos\left(\frac{\theta_{s\eta}}{2}\right) \\ \sin\left(\frac{\theta_{s\eta}}{2}\right)\frac{p_+}{p} \end{pmatrix}\frac{e^{i\mathbf{p}\cdot\mathbf{r}/\hbar}}{\sqrt{S}}, \tag{4}$$

where $p_+ = \eta p_x + ip_y$; $p = |\mathbf{p}|$, and S is the monolayer area. In Eq. (4),

$$\cos\theta_{s\eta} = \frac{\Delta - s\eta(\lambda_v - \lambda_c)}{2\sqrt{\left[\frac{\Delta - s\eta(\lambda_v - \lambda_c)}{2}\right]^2 + v^2p^2}}. \tag{5}$$

Two spin-resolved branches described by Eq. (3) cross if $\lambda_v > 0$ and $\lambda_c < 0$, as it is the case for MoS_2 monolayer [15]. Expanding the energy in (3) for small momenta $vp \ll \Delta$ gives the spin-dependent energy branches in effective-mass representation,

$$E_{\eta,s}(\mathbf{p}) \approx \frac{\Delta}{2} - \eta s|\lambda_c| + \frac{\mathbf{p}^2}{2m_{\eta,s}}, \quad \frac{1}{m_{\eta,s}} = \frac{2v^2}{\Delta - \eta s\lambda_v}, \tag{6}$$

where the term proportional to λ_c was omitted in the expression for the effective mass due to its smallness, $|\lambda_c| \ll \lambda_v$ [45].

III. SPIN-LATTICE INTERACTION DUE TO RAYLEIGH SAW

A. Rayleigh SAW interaction with electron spin

Let us assume the dielectric substrate surface with MoS_2 monolayer corresponds to the plane $z = 0$ with the axis z directed out of the bulk of the substrate. The monolayer is of n type; thus the Fermi level lies in the conduction band. Rayleigh SAWs propagating along the substrate surface create longitudinal and transverse deformations. For simplicity, we assume an isotropic substrate, and thus the wave equation for Rayleigh SAWs in terms of the substrate displacement vector $\mathbf{u}$ reads [46],

$$\ddot{\mathbf{u}} = c_t^2\Delta\mathbf{u} + (c_l^2 - c_t^2)\text{grad div }\mathbf{u}, \tag{7}$$

where c_l and c_t are longitudinal and transverse sound velocities, respectively. If the SAW propagates in the $\hat{x}$ direction, the displacement vector $\mathbf{u}(\mathbf{r},t)$ has the following components [47]:

$$\begin{aligned} u_x(z) &= (kBe^{\kappa_l z} + \kappa_t Ae^{\kappa_t z})e^{ikx - i\omega t}, \quad u_y = 0, \\ u_z(z) &= (-i\kappa_l Be^{\kappa_l z} - ikAe^{\kappa_t z})e^{ikx - i\omega t}, \end{aligned} \tag{8}$$

where

$$\kappa_l = \sqrt{k^2 - \omega^2/c_l^2}, \quad \kappa_t = \sqrt{k^2 - \omega^2/c_t^2}, \quad k = |\mathbf{k}|, \tag{9}$$

and

$$A = \frac{\sqrt{I_0}}{\omega\sqrt{c_t\chi\rho\kappa}}, \quad B = -\frac{2\sqrt{1-\xi^2}}{(2-\xi^2)}\frac{\sqrt{I_0}}{\omega\sqrt{c_t\chi\rho\kappa}}, \tag{10}$$

where

$$\kappa = \frac{2(1-\chi^2)}{k_l(2-\chi^2)^2}(k_l^2 + k^2) + \frac{k^2 + k_t^2}{2k_t} - \frac{4\sqrt{1-\chi^2}k}{(2-\chi^2)}. \tag{11}$$

Here χ is a constant characterizing the SAW dispersion in such a way that $\omega = c_t\chi k$, I_0 is the SAW intensity, $\mathbf{k}$ is the SAW wave vector, and ρ is the density of the substrate material [47].

We consider a standard experimental setup consisting of the substrate and a TMD monolayer attached to its surface. The strain field produced by SAWs traveling along the substrate is directly transferred to the monolayer lattice. The

SAW-induced strain field appearing in the monolayer is due to the molecular coupling between the latter and the substrate. Since the wavelength of the SAW is large enough, the theoretical description of the system can be based on the classical continuity equations for the components of the stress tensor in the substrate and the monolayer [36]. Such an approximation simplifies the theoretical consideration of mechanical deformations, independent of the microscopic nature of the molecular forces.

The Hamiltonian capturing the effects of strain and curvature to the spin dynamics of electrons in TMDs in terms of the out-of-plane displacement u_z at $z = 0$ reads as [48]

$$V(\mathbf{r},t) = \begin{pmatrix} \eta\mathbf{s}\cdot\mathbf{B}_c(\mathbf{r},t) & \beta(i\hat{s}_x + \eta\hat{s}_y)\nabla^2 u_z \\ \beta(-i\hat{s}_x + \eta\hat{s}_y)\nabla^2 u_z & \eta\mathbf{s}\cdot\mathbf{B}_v(\mathbf{r},t) \end{pmatrix}, \quad (12)$$

where $\hat{s}_i$ are Pauli spin matrices, ∇^2 is the Laplace operator, and $\mathbf{B}_c(\mathbf{r},t)$ and $\mathbf{B}_v(\mathbf{r},t)$ are effective magnetic fields expressing the interaction between deformation field and the spin degree of freedom for electrons in TMD monolayers in the conduction (c) and valence (v) band, respectively:

$$\mathbf{B}_c(\mathbf{r},t) = \left[2\xi_x^c \partial_{xy}^2 u_z, \xi_y^c\left(\partial_x^2 - \partial_y^2\right)u_z(z=0), 0\right],$$
$$\mathbf{B}_v(\mathbf{r},t) = \left[2\xi_x^v \partial_{xy}^2 u_z, \xi_y^v\left(\partial_x^2 - \partial_y^2\right)u_z(z=0), 0\right]. \quad (13)$$

The deformation constants β and $\xi_{x,y}^{c,v}$ describe the strength of spin-strain interaction [48]. Thus the interaction of a Rayleigh SAW with a MoS_2 lattice takes place due to the coupling of spin with strain-induced effective magnetic fields.

Substituting Eq. (8) and Eq. (13) in Eq. (12) yields

$$V(\mathbf{r},t) = -\eta k^2(i\kappa_l B + ikA)\begin{pmatrix} \xi_c\hat{s}_y & i\beta\hat{s}_- \\ -i\beta\hat{s}_+ & \xi_v\hat{s}_y \end{pmatrix} e^{ikx - i\omega t}, \quad (14)$$

where $\hat{s}_\pm = \hat{s}_x \pm i\hat{s}_y$. Finding the conduction-band eigenfunctions, $\Psi_{s,\eta}(\mathbf{p})$, from Eq. (4) in the limit $vp \ll \Delta$ and using Eqs. (14) and (3) allows us to find the transition matrix element capturing the spin-lattice interaction,

$$M_{s',s}^{\eta}(\mathbf{p}',\mathbf{p}) = \eta k^2 \xi_c \langle s'|\hat{s}_y|s\rangle(i\kappa_l B + ikA) \times \frac{(2\pi)^2}{S}\delta\left(\frac{\mathbf{p}}{\hbar} + \mathbf{k} - \frac{\mathbf{p}'}{\hbar}\right), \quad (15)$$

or

$$\left|M_{s',s}^{\eta}(\mathbf{p}',\mathbf{p})\right|^2 = |M_0|^2\delta^2\left(\frac{\mathbf{p}}{\hbar} + \mathbf{k} - \frac{\mathbf{p}'}{\hbar}\right)\frac{(2\pi)^4}{S^2}, \quad (16)$$

where $|M_0|^2 = k^4\xi_c^2|\kappa_l B + kA|^2$ only depends on the parameters of the Rayleigh SAW.

B. Spin-acoustic resonance

The transition rate from an initial state $|\eta, s, \mathbf{p}\rangle$ to the final state $|\eta, s', \mathbf{p}'\rangle$ in a valley η obeys the Fermi golden rule,

$$g_{s's}^{\eta}(\mathbf{p}',\mathbf{p}) = \frac{2\pi}{\hbar}\sum_{\mathbf{p}'\mathbf{p}}\left|M_{s's}^{\eta}(\mathbf{p}',\mathbf{p})\right|^2[f_{\eta s}(\mathbf{p}) - f_{\eta s'}(\mathbf{p}')] \times \delta(E_{\eta s'}(\mathbf{p}') - E_{\eta s}(\mathbf{p}) - \hbar\omega). \quad (17)$$

Substituting Eq. (16) in Eq. (17), and then converting the summation over $\mathbf{p}'$ to an integration and using the translation property of the δ function yields

$$g_{s's}^{\eta}(\mathbf{p}) = \frac{2\pi}{\hbar}|M_0|^2 \mathrm{W}_\eta, \quad (18)$$

where

$$\mathrm{W}_\eta = \sum_{\mathbf{p}}[f_{\eta s}(\mathbf{p}) - f_{\eta s'}(\mathbf{p}+\hbar\mathbf{k})] \times \delta[E_{\eta s'}(\mathbf{p}+\hbar\mathbf{k}) - E_{\eta s}(\mathbf{p}) - \hbar\omega]. \quad (19)$$

With account of electron relaxation, the δ function transforms into a Lorentzian and then the transition probability reads

$$\mathrm{W}_\eta = \frac{\hbar}{\pi\tau}\sum_{\mathbf{p}}\frac{f_{\eta s}(\mathbf{p}) - f_{\eta s'}(\mathbf{p}+\hbar\mathbf{k})}{(E_{\eta s'}(\mathbf{p}+\hbar\mathbf{k}) - E_{\eta s}(\mathbf{p}) - \hbar\omega)^2 + \left(\frac{\hbar}{\tau}\right)^2}, \quad (20)$$

where we used the phenomenological relaxation time, τ, without considering the details of a particular microscopic mechanism of electron relaxation. Following the work [49], we consider τ to be an effective parameter which accounts for all the relaxation effects. From the general perspective, the electron relaxation time in our theory is the spin-flip time. The microscopic nature of spin-flip relaxation processes may be due to both intra- and intervalley electron transitions. A detailed analysis of all the effects which contribute to τ deserves a separate study and is a topic of recent research.

In the above expressions, $f_{\eta,s(s')} = [e^{(E_{\eta,s(s')} - \varepsilon_F)/k_BT} + 1]^{-1}$ is the Fermi distribution function for the spin-polarized electrons in the spin-split subbands. We can find W_η in Eq. (20) numerically to obtain the transition probability, and the results are shown as a function of SAW frequency in Figs. 2(c) and 2(d).

For analytical results, writing the Fermi distribution functions in the low-temperature limit and substituting the energies gives [50]

$$\mathrm{W}_\eta = \frac{\hbar}{\tau\pi}\sum_{\mathbf{p}}\left[\Theta\left(\varepsilon_F - \frac{\mathbf{p}^2}{2m_{\eta,s}}\right) - \Theta\left(\varepsilon_F - \frac{(\mathbf{p}+\hbar\mathbf{k})^2}{2m_{\eta,s'}} - 2|\lambda_c|\right)\right] \times \frac{1}{\left(\frac{(\mathbf{p}+\hbar\mathbf{k})^2}{2m_{\eta,s'}} + 2|\lambda_c| - \frac{\mathbf{p}^2}{2m_{\eta,s}} - \hbar\omega\right)^2 + (\hbar/\tau)^2}. \quad (21)$$

Let us note that the k-dependent terms in Eq. (21) can be omitted in the limit $vk\tau \sim lk \ll 1$, where l is electron mean free path.

The second θ function in Eq. (21) vanishes when $\varepsilon_F < 2|\lambda_c|$, categorizing spin-flip transitions in two distinct regimes: (i) transitions, which occur when only the lower band is filled ($\varepsilon_F < 2|\lambda_c|$) and (ii) when both the bands are filled ($\varepsilon_F > 2|\lambda_c|$). Performing the integration in Eq. (21) yields

$$\mathrm{W}_\eta = \frac{\mu S}{2\pi^2\hbar^2}\left\{\arctan\left[\left(\hbar\omega - 2|\lambda_c| + \frac{m_{\eta,s}}{\mu}\varepsilon_F\right)\frac{\tau}{\hbar}\right] - \arctan\left[(\hbar\omega - 2|\lambda_c|)\frac{\tau}{\hbar}\right]\right\} \quad (22)$$

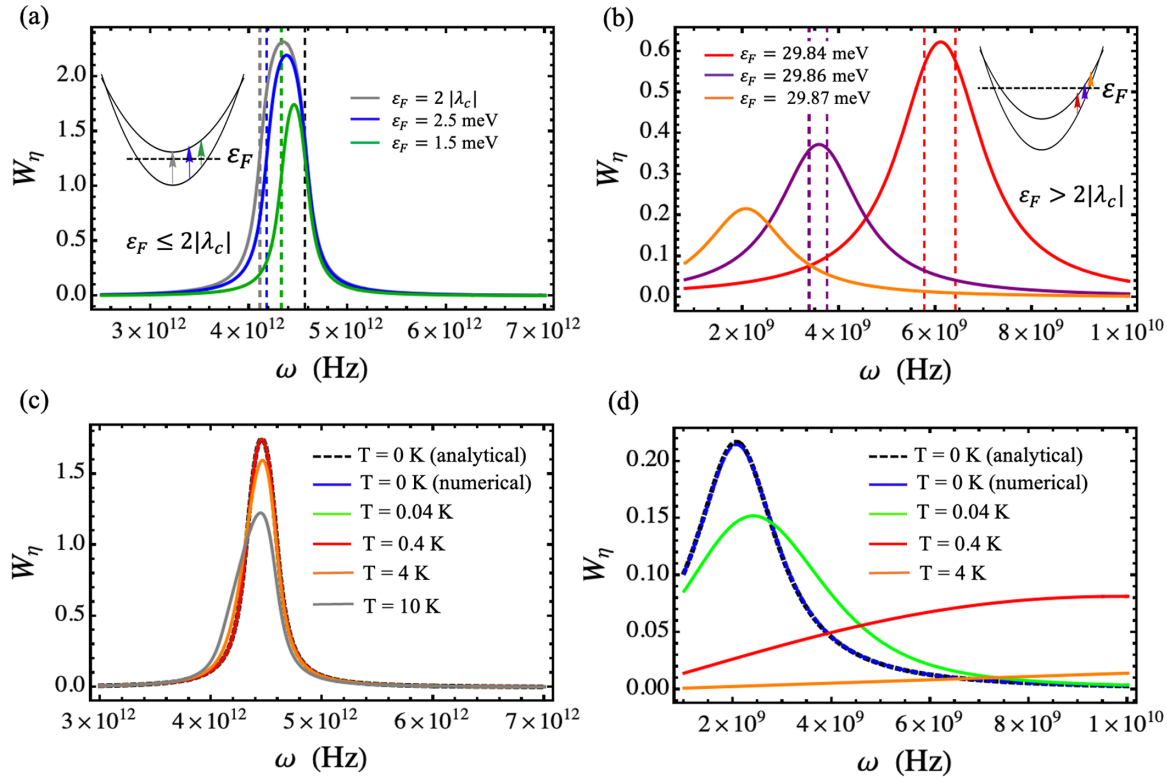

FIG. 2. Panels (a) and (b): Analytical results for normalized transition probability $W_\eta/(\mu S/2\pi^2\hbar^2)$ as a function of SAW frequency at zero temperature. The vertical lines correspond to the cut-off frequencies at the onsets of resonances for $2|\lambda_c| - \varepsilon_F m_{\eta,s}/\mu$. Offset of resonance occurs in (a) at a common frequency $2|\lambda_c|$ (black grid line) and in (b) at $(2|\lambda_c| - \frac{m_{\eta,s}}{\mu}\varepsilon_F)\frac{m_{\eta,s'}}{m_{\eta,s}}$ (grid lines of corresponding colors). The corresponding spin-flip transitions are depicted in the same colors in the inset plots. Panels (c) and (d): Numerical results for normalized transition probability at different temperatures.

for $\varepsilon_F \leqslant 2|\lambda_c|$, and

$$W_\eta = \frac{\mu S}{2\pi^2\hbar^2}\left\{\arctan\left[\left(\hbar\omega - 2|\lambda_c| + \frac{m_{\eta,s}}{\mu}\varepsilon_F\right)\frac{\tau}{\hbar}\right] - \arctan\left[\left[\hbar\omega - 2|\lambda_c| + \frac{m_{\eta,s'}}{\mu}(\varepsilon_F - 2|\lambda_c|)\right]\frac{\tau}{\hbar}\right]\right\} \tag{23}$$

for $\varepsilon_F > 2|\lambda_c|$, where μ is the reduced mass $(1/\mu) = (1/m_{\eta,s}) - (1/m_{\eta,s'})$, which is equal in both of the valleys. Also, note that $W_{\eta=1} = W_{\eta=-1}$.

Figure 2 shows the behavior of transition probabilities described by Eqs. (22) and (23). Panel (a) corresponds to Eq. (22), whereas panel (b) demonstrates Eq. (23). Adjusting the Fermi level ε_F via the electron density, we obtain the curves for transition probability in Fig. 2(a) for $\varepsilon_F \sim 2$ meV at $\tau = 10^{-11}$ s and in Fig. 2(b) $\varepsilon_F \sim 30$ meV at $\tau = 10^{-9}$ s. The value of spin-orbit splitting is taken as $|\lambda_c| = 1.5$ meV for MoS_2 monolayer [15]. In both cases, the onset of SAR occurs at SAW frequency $\omega = 2|\lambda_c| - (m_{\eta,s}/\mu)\varepsilon_F$. However, the upper cutoff of the frequency is different: while in Fig. 2(a) it is always $2|\lambda_c|$, irrespective of the Fermi energy, in Fig. 2(b) the cutoff depends on the Fermi energy, $\omega = (2|\lambda_c| - (m_{\eta,s}/\mu)\varepsilon_F)(m_{\eta,s}/m_{\eta,s'})$. Thus the SAW frequency should satisfy the condition

$$2|\lambda_c| - \frac{m_{\eta,s}}{\mu}\varepsilon_F \leqslant \omega \leqslant \left(2|\lambda_c| - \frac{m_{\eta,s}}{\mu}\varepsilon_F\right)\frac{m_{\eta,s}}{m_{\eta,s'}}. \tag{24}$$

Panels (a) and (b) show contrasting dependence of the height and the width of the resonances on the Fermi energy: while in panel (a) ($\varepsilon_F < 2|\lambda_c|$) the height and the width of each peak increase with the increase of Fermi energy (indicating an increasing probability of resonant transitions over a wider range of SAW frequencies), in panel (b) ($\varepsilon_F > 2|\lambda_c|$), this probability decreases with the increase of the Fermi energy, and it ultimately goes to zero when the Fermi energy reaches the point of subbands crossing.

We note that resonant spin-flip transitions occur at SAW frequencies determined by the energy difference between the subbands [see Figs. 2(a) and 2(b) inset]. As a consequence, the SAW frequency required for resonant transition from the bottom of the band is much higher ($\sim 10^{12}$ Hz) than for transitions close to band crossings ($\sim 10^9$ Hz). These values of relaxation time are taken so that the clean limit ($\omega\tau > 1$) is satisfied to achieve the SAR resonance conditions. Since SAW experiments usually operate with MHz to GHz frequencies, let us focus on the case $\varepsilon_F > 2|\lambda|_c$, where the Fermi level is close to the band-crossing point. Hence we use Eq. (23) [and not Eq. (22)] in our further analysis.

Figures 2(c) and 2(d) show the transition probabilities for different values of temperature after direct numerical integration of Eq. (20). We note that at zero temperature, the numerical results match the analytical results exactly. With the increase of temperature, the resonance peaks start to smear out. The smearing effect is more pronounced in the regime $\varepsilon_F > 2|\lambda_c|$ as compared to $\varepsilon_F < 2|\lambda_c|$.

Furthermore, the energy absorbed per unit time as a result of the spin-lattice interaction can be found after substituting W_η in Eq. (18) and multiplying this expression by a quantum of energy $\hbar\omega$:

$$\mathrm{Q}_\eta = |M_0|^2 \frac{\mu S}{\pi\hbar^3}\hbar\omega\left\{\arctan\left[\left(\hbar\omega - 2|\lambda_c| + \frac{m_{\eta,s}}{\mu}\varepsilon_F\right)\frac{\tau}{\hbar}\right] - \arctan\left[\left[\hbar\omega - 2|\lambda_c| + \frac{m_{\eta,s'}}{\mu}(\varepsilon_F - 2|\lambda_c|)\right]\frac{\tau}{\hbar}\right]\right\}. \tag{25}$$

Since $\mathrm{W}_{\eta=1} = \mathrm{W}_{\eta=-1}$, therefore $\mathrm{Q}_{\eta=1} = \mathrm{Q}_{\eta=-1}$ also.

C. Valley degeneracy breaking

Applying an external magnetic field in $\hat{z}$ direction yields a Zeeman shift of $\Delta_B = g\mu_B B$, where g is the TMD monolayer electron g factor, B is the magnitude of the external magnetic field and μ_B is the Bohr magneton. The part of the Hamiltonian accounting for the spin angular momentum of electrons reads

$$H_B = -\Delta_B \sigma_0 s_z, \tag{26}$$

and thus the full Hamiltonian transforms into

$$H = \begin{pmatrix} \Delta/2 + \eta\lambda_c s - \Delta_B s & v(\eta p_x - i p_y) \\ v(\eta p_x + i p_y) & -\Delta/2 + \eta\lambda_v s - \Delta_B s \end{pmatrix}. \tag{27}$$

The energy of the spin-split subbands of the conduction band then reads

$$E_{\eta,s}(p) \approx \frac{\Delta}{2} - \eta s|\lambda_c| + \frac{\mathbf{p}^2}{2m_{\eta,s}} - s\Delta_B, \tag{28}$$

where a similar approximation as in Eq. (6) was employed. Following the analytical calculations in the zero-temperature limit as in the previous section gives the modified transition probability, W^B_η, which now accounts for the external magnetic field (for $\varepsilon_F > 2|\lambda_c|$)

$$\mathrm{W}^B_{\eta=+1} = \frac{\mu}{2\pi\hbar^2}\left\{\arctan\left[\left(\frac{m_{1,1}}{\mu}\varepsilon_F + \hbar\omega - 2(|\lambda_c| + \Delta_B)\right)\frac{\tau}{\hbar}\right] - \arctan\left[\left(\frac{m_{1,-1}}{\mu}[\varepsilon_F - 2(|\lambda_c| + \Delta_B)] + \hbar\omega - 2(|\lambda_c| + \Delta_B)\right)\frac{\tau}{\hbar}\right]\right\}, \tag{29}$$

and

$$\mathrm{W}^B_{\eta=-1} = \frac{\mu}{2\pi\hbar^2}\left\{\arctan\left[\left(\frac{m_{-1,-1}}{\mu}\varepsilon_F + \hbar\omega - 2(|\lambda_c| - \Delta_B)\right)\frac{\tau}{\hbar}\right] - \arctan\left[\left(\frac{m_{-1,1}}{\mu}[\varepsilon_F - 2(|\lambda_c| - \Delta_B)] + \hbar\omega - 2(|\lambda_c| - \Delta_B)\right)\frac{\tau}{\hbar}\right]\right\}. \tag{30}$$

Evidently, the transition probabilities differ in both valleys. This difference stems from the Zeeman splittings, which are different for different valleys.

Figure 3(a) shows the valley-dependent transition probabilities defined in Eqs. (29) and (30) as functions of applied SAW frequency. At $B = 0$ the curves corresponding to different valleys overlap (black curve), and they start deviating towards opposite sides of the frequency spectrum after the magnetic field is turned on. This deviation increases for higher magnitudes of magnetic field. SAR peak frequency for the K valley undergoes a redshift, as in this valley the distance between the spin-split subbands increases from $2|\lambda_c| \to 2(|\lambda_c| + \Delta_B)$, thus requiring higher energy for the transition to occur. For similar reasons, the peak frequency in the K' valley undergoes a blueshift, as in this valley the intersubband distance decreases, $2|\lambda_c| \to 2(|\lambda_c| - \Delta_B)$. Moreover, the line shape of SAR remains the same for both the valleys (green and red curves). The deviations of these curves from the black curve (SAR curve in the valley degenerate case) are symmetrical in each valley.

Figure 3(b) shows the dependence of spin-flip transition probabilities on magnitude of applied magnetic field at certain fixed frequencies. These probabilities are equal when $B = 0$ (red and green curves start from the same point), and the curves start deviating from each other once B is turned on. At some magnitudes of magnetic field (of the order of few mT), SAR peaks experience their maxima, which depend on the SAW frequency. Furthermore, the curves are asymmetrical. Increasing B up to ∼20 mTs results in vanishing of W^B_η, indicating that spin-flip transitions are suppressed. The energy absorbed in both valleys experiences a similar valley-dependence behavior as $\mathrm{W}^{\mathrm{B}}_\eta$: $\mathrm{Q}^{\mathrm{B}}_{\mathrm{K}} \sim \omega \mathrm{W}^{\mathrm{B}}_{\mathrm{K}}$ and $\mathrm{Q}^{\mathrm{B}}_{\mathrm{K}'} \sim \omega \mathrm{W}^{\mathrm{B}}_{\mathrm{K}'}$.

When thermal occupation of the spin-split states is considered, the resonance peaks in both valleys become smeared out with increasing temperature. At temperatures $T \sim 4$ K or higher, the spin-acoustic resonance vanishes (see Fig. 4).

IV. ACOUSTOELECTRIC CURRENT

The SAW-induced spin-flip transitions result in an emergence of electric current in the system due to the imbalance

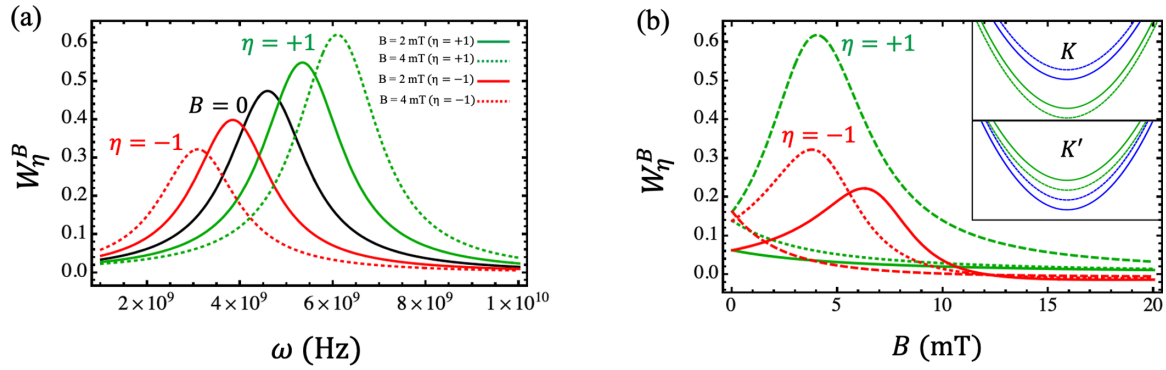

FIG. 3. Illustration of the valley degeneracy breaking of the spin-split subbands in the presence of Zeeman splitting: The modified transition probability as a function of the SAW frequency (a) and the magnitude of external magnetic field (b) for the valley index $\eta = +1$ (green) and $\eta = -1$ (red). (a) The solid lines correspond to $B = 2$ mT, and the dotted lines correspond to $B = 4$ mT. The black line corresponds to the case of zero magnetic field. (b) Curves of different colors correspond to different SAW frequencies: 2 GHz (solid), 3 GHz (dotted), and 6 GHz (dashed). Inset in (b) shows spin-split subbands having spin-up (green) and spin-down (blue) spins, before (solid) and after (dashed) application of external magnetic field.

of electron populations in the spin-split subbands. The SAW transfers its momentum to the electrons under spin-flip transitions caused by the spin-SAW interaction and corresponding SAW-phonon absorption. The current density can be found using the standard expression [49]

$$\boldsymbol{j}_\eta = \frac{2\pi e}{S\hbar}\sum_{\mathbf{p},\mathbf{p}'}\tau\left[\boldsymbol{v}^\eta_{\mathbf{p}',s'} - \boldsymbol{v}^\eta_{\mathbf{p},s}\right]\left|M^\eta_{s',s}(\mathbf{p}',\mathbf{p})\right|^2[f(E_{\eta,s}(\mathbf{p})) - f(E_{\eta,s'}(\mathbf{p}'))]\delta(E_{\eta s'}(\mathbf{p}') - E_{\eta,s}(\mathbf{p}) - \hbar\omega), \tag{31}$$

where $\boldsymbol{v}^\eta_{\mathbf{p},s} = dE_{\eta,s}(\mathbf{p})/d\mathbf{p}$ is the electron velocity in the corresponding spin-resolved subband.

Integrating over $\mathbf{p}'$ in the regime $vk\tau \sim lk \ll 1$, as before, and thus expanding the distribution and the $\delta-$ functions for small $\mathbf{k}$ gives [50]

$$\begin{aligned}\boldsymbol{j}_\eta = &-C\int d\mathbf{p}\frac{\mathbf{p}}{\mu}[f(E_{\eta,s}(p)) - f(E_{\eta,s'}(p))]\\ &\times \hbar\mathbf{k}\cdot\nabla_{\mathbf{p}}\delta(E_{\eta,s'}(p) - E_{\eta,s}(p) - \hbar\omega)\\ &+ C\int d\mathbf{p}\frac{\mathbf{p}}{\mu}\delta(E_{\eta,s'}(p) - E_{\eta,s}(p) - \hbar\omega)\\ &\times [\hbar\mathbf{k}\cdot\nabla_{\mathbf{p}}f(E_{\eta,s'}(p))],\end{aligned} \tag{32}$$

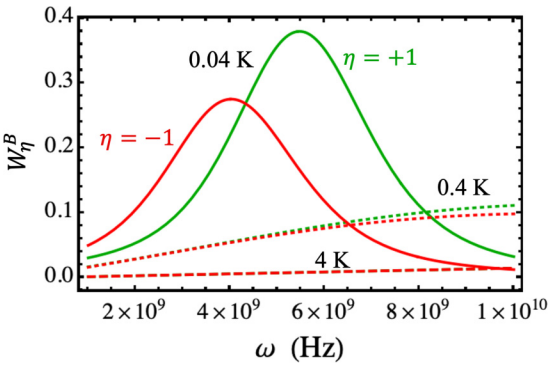

FIG. 4. Effect of temperature on valley degeneracy breaking. Transition probability in the presence of external magnetic field $B = 2$ mT at temperature 0.04 K (solid), 0.4 K (dotted), and 4 K (dashed) for $\eta = 1$ (green) and $\eta = -1$ (red).

where

$$C = \frac{2\pi e}{\hbar}\tau\frac{|M_0|^2}{2\pi\hbar^2}. \tag{33}$$

Accounting for relaxation processes requires the δ functions to be replaced by Lorentzians. In the low-temperature limit, analytical calculations give two contributions to AE current flowing in the $\hat{x}$ direction,

$$j^{(a)}_\eta = j_0\arctan\left[\frac{\frac{1-\epsilon_\lambda}{a'} + \epsilon_\Omega}{\epsilon_\tau}\right] - j_0\arctan\left[\frac{\frac{1}{a} + \epsilon_\Omega}{\epsilon_\tau}\right], \tag{34}$$

$$j^{(b)}_\eta = -j_0\frac{2}{a}\left(1 + \frac{2}{\epsilon_T}\ln 2\right)\frac{1/\epsilon_\tau}{\left(\frac{1}{a} + \epsilon_\Omega\right)^2/\epsilon_\tau^2 + 1}, \tag{35}$$

where the SAW wave vector is assumed to be pointing to $\mathbf{k} = (k_x, 0)$,

$$j_0 = C\frac{\hbar k_x}{\mu}\frac{2\mu}{\pi}, \tag{36}$$

which is valley independent, and the dimensionless parameters read

$$\epsilon_F\beta = \frac{\varepsilon_F}{k_BT} = \epsilon_T, \quad \frac{\hbar}{\tau\epsilon_F} = \epsilon_\tau, \quad \frac{2|\lambda_c|}{\varepsilon_F} = \varepsilon_\lambda,$$
$$\frac{\hbar\omega - 2|\lambda_c|}{\epsilon_F} = \epsilon_\Omega, \quad a' = \frac{\mu}{m_{\eta,s'}}, \quad a = \frac{\mu}{m_{\eta,s}}. \tag{37}$$

We note that the first contribution in Eq. (32) primarily comes from the difference of the populations of spins in two subbands. The second contribution comes from the gradient of population distribution in one band. Hence, a possible physical origin of the two contributions of the AE current are intersubband [Eq. (34)] and intrasubband [Eq. (35)] processes in the acoustoelectric current.

The current in the presence of magnetic field has the same form; however, $2|\lambda_c|$ entering Eqs. (34) and (35) via ϵ_λ should be replaced by

$$\text{K valley:} \quad 2|\lambda_c| \longrightarrow 2(|\lambda_c| + \Delta_B), \tag{38}$$

$$\text{K}' \text{ valley:} \quad 2|\lambda_c| \longrightarrow 2(|\lambda_c| - \Delta_B). \tag{39}$$

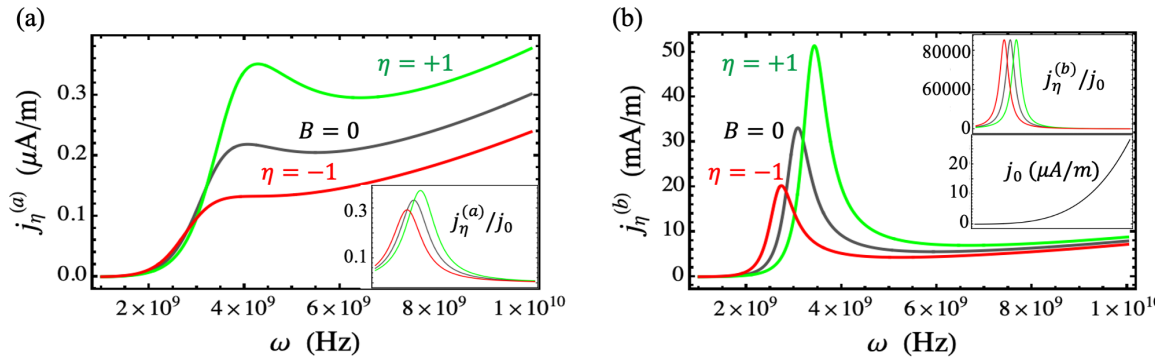

FIG. 5. Two contributions of the acoustoelectric current before and after the application of external magnetic field in K and K′ valley as functions of frequency of the SAW. Insets in (a) and (b) (upper inset) show the sole contribution due to valley-dependent parts of the respective currents. Lower inset of (b) shows only the valley-independent part, j_0.

Since j_0 does not depend on the splitting parameter $2|\lambda_c|$ originating from SOC, it is not affected by valley degeneracy breaking.

Figure 5 shows two contributions to AE current. Both $j_\eta^{(a)}$ and $j_\eta^{(b)}$ depend on frequency through (i) the factor j_0 and (ii) other terms in corresponding equations. The factor j_0 is directly proportional to ω via the wave vector k. Evidently, it vanishes as k goes to zero; thus both contributions to electric current are of drag nature.

However, the dependence of $j_\eta^{(a)}$ and $j_\eta^{(b)}$ on frequency is more complicated than that of j_0, which becomes clear from the comparison of the main plots and insets in both panels of Fig. 5. Also, all the dependence on the valley parameter lies in (ii) terms. Furthermore, it should be mentioned that the overall magnitude of $j_\eta^{(b)}$ turns out orders of magnitude higher than $j_\eta^{(a)}$, and thus the latter can be disregarded.

V. CONCLUSIONS AND OUTLOOK

In a 2D MoS_2 monolayer exposed to a Rayleigh surface acoustic wave there can occur a spin-acoustic resonance accompanied by the onset of acoustoelectric current in the system. Moving the doping level allows for the spin-acoustic resonance to happen in two distinct frequency ranges, depending on the relation between the Fermi level ε_F and the spin-orbit splitting λ_c: (i) at hypersound frequencies for $\varepsilon_F < |2\lambda_c|$, and (ii) at GHz frequencies for $\varepsilon_F > 2|\lambda_c|$. The latter case, which occurs for electron momenta close to the subband crossing point, seems more accessible from an experimental viewpoint due to the frequency range. The value of Fermi energy in the vicinity of the crossing point of spin-resolved subbands corresponds to high electron densities. According to our estimations, for MoS_2 it is of the order of $n \approx 10^{13} - 10^{14}$ cm^{-2}. However, such densities are still accessible in modern experiments on TMD monolayers [51,52].

In the presence of the time-reversal symmetry in the system, the resonance and the acoustoelectric current take place in both the valleys at the same SAW frequencies. An application of an external magnetic field, producing different Zeeman splittings in different valleys, results in valley-dependent behavior of spin-acoustic resonance and the energy absorbed by the system. Valley-dependent spin-acoustic resonance peaks are observed at applied magnetic fields of few mTs and vanish when magnetic fields are increased to around 20 mT. Increasing the temperature, the resonance peaks start smearing out. The valley degeneracy breaking no longer occurs when temperature reaches around 4 K. This indicates that the observation of valley spin-acoustic resonance might only be limited to low-temperature experiments. The acoustoelectric current comprises two parts, originating from intersubband and intrasubband contributions. The spectrum of current density manifests distinct behavior for the two contributions, with magnitudes differing by three orders of magnitude.

The other possible way to lift the valley degeneracy is the illumination of the TMD monolayer sample by an external electromagnetic field. The specific valley-selective optical transition rules [8,53] result in inequivalent valley populations and thus produce different currents in different valleys, even in the absence of an external magnetic field. In this case the photoinduced valley spin-acoustic resonance can take place in the absence of external Zeeman field. Thus, the effects considered here may serve in acoustoelectric spectroscopy of the valley-selective phenomena as an additional tool to monitor valley physics in TMD monolayer materials.

ACKNOWLEDGMENT

We acknowledge support from the Institute for Basic Science in Korea (Project No. IBS-R024-D1) and the Foundation for the Advancement of Theoretical Physics and Mathematics "BASIS."

[1] K. F. Mak, C. Lee, J. Hone, J. Shan, and T. F. Heinz, Atomically Thin MoS_2: A New Direct-Gap Semiconductor, Phys. Rev. Lett. **105**, 136805 (2010).

[2] A. Kormányos, V. Zólyomi, N. D. Drummond, P. Rakyta, G. Burkard, and V. I. Fal'ko, Monolayer MoS_2: Trigonal warping, the Γ valley, and spin-orbit coupling effects, Phys. Rev. B **88**, 045416 (2013).

[3] Z. Wu, B. T. Zhou, X. Cai, P. Cheung, G.-B. Liu, M. Huang, J. Lin, T. Han, L. An, Y. Wang, S. Xu, G. Long, C. Cheng, K. T. Law, F. Zhang, and N. Wang, Intrinsic valley

Hall transport in atomically thin MoS_2, Nat. Commun. **10**, 1 (2019).

[4] A. V. Kalameitsev, V. M. Kovalev, and I. G. Savenko, Valley Acoustoelectric Effect, Phys. Rev. Lett. **122**, 256801 (2019).

[5] K. Sonowal, A. V. Kalameitsev, V. M. Kovalev, and I. G. Savenko, Acoustoelectric effect in two-dimensional Dirac materials exposed to Rayleigh surface acoustic waves, Phys. Rev. B **102**, 235405 (2020).

[6] A. J. Pearce and G. Burkard, Electron spin relaxation in a transition-metal dichalcogenide quantum dot, 2D Mater. **4**, 025114 (2017).

[7] K. F. Mak and J. Shan, Photonics and optoelectronics of 2D semiconductor transition metal dichalcogenides, Nat. Photon. **10**, 216 (2016).

[8] A. Srivastava, M. Sidler, A. V. Allain, D. S. Lembke, A. Kis, and A. Imamoğlu, Valley Zeeman effect in elementary optical excitations of monolayer WSe_2, Nat. Phys. **11**, 141 (2015).

[9] D. Ko, A. V. Morozov, V. M. Kovalev, and I. G. Savenko, Optical valleytronics of impurity states in two-dimensional Dirac materials, Phys. Rev. B **103**, L161301 (2021).

[10] G. Wang, C. Robert, A. Suslu, B. Chen, S. Yang, S. Alamdari, I. C. Gerber, T. Amand, X. Marie, S. Tongay, and B. Urbaszek, Spin-orbit engineering in transition metal dichalcogenide alloy monolayers, Nat. Commun. **6**, 10110 (2015).

[11] Z. Wang, A. Molina-Snchez, P. Altmann, D. Sangalli, D. De Fazio, G. Soavi, U. Sassi, F. Bottegoni, F. Ciccacci, M. Finazzi, L. Wirtz, A. C. Ferrari, A. Marini, G. Cerullo, and S. Dal Conte, Intravalley spin-flip relaxation dynamics in single-layer WS_2, Nano Lett. **18**, 6882 (2018).

[12] A. V. Parafilo, M. V. Boev, V. M. Kovalev, and I. G. Savenko, Photogalvanic transport in fluctuating Ising superconductors, Phys. Rev. B **106**, 144502 (2022).

[13] D. Xiao, G.-B. Liu, W. Feng, X. Xu, and W. Yao, Coupled Spin and Valley Physics in Monolayers of MoS_2 and Other Group-VI Dichalcogenides, Phys. Rev. Lett. **108**, 196802 (2012).

[14] K. Kosmider, J. W. Gonzalez, and J. Fernandez-Rossier, Large spin splitting in the conduction band of transition metal dichalcogenide monolayers, Phys. Rev. B **88**, 245436 (2013).

[15] A. Kormányos, G. Burkard, M. Gmitra, J. Fabian, V. Zólyomi, N. D. Drummond, and V. Fal'ko, $\mathbf{k}\cdot\mathbf{p}$ theory for two-dimensional transition metal dichalcogenide semiconductors, 2D Mater. **2**, 022001 (2015).

[16] G.-B. Liu, W.-Y. Shan, Y. Yao, W. Yao, and D. Xiao, Three-band tight-binding model for monolayers of group-VIB transition metal dichalcogenides, Phys. Rev. B **88**, 085433 (2013).

[17] Z. Y. Zhu, Y. C. Cheng, and U. Schwingenschlögl, Giant spin-orbit-induced spin splitting in two-dimensional transition-metal dichalcogenide semiconductors, Phys. Rev. B **84**, 153402 (2011).

[18] A. Hernández-Mínguez, A. V. Poshakinskiy, M. Hollenbach, P. V. Santos, and G. V. Astakhov, Anisotropic Spin-Acoustic Resonance in Silicon Carbide at Room Temperature, Phys. Rev. Lett. **125**, 107702 (2020).

[19] S. A. Al'tshuler, B. I. Kochelaev, and A. M. Leushin, Paramagnetic absorption of sound, Sov. Phys. Usp. **4**, 880 (1962).

[20] F. B. Fidler and J. W. Tucker, Quantum theory of ultrasonic absorption due to spin-phonon interactions in concentrated paramagnetic crystals, J. Phys. C **3**, 1877 (1970).

[21] C. A. Bates, L. C. Goodfellow, and K. W. H. Stevens, The theory of acoustic paramagnetic resonance of v^{3+} in MgO, J. Phys. C **3**, 1831 (1970).

[22] H. F. Lockwood, K. F. Etzold, and B. Josephson, Acoustic Paramagnetic Resonance in Arsenic-Doped Germanium, Phys. Rev. Lett. **21**, 1471 (1968).

[23] J. G. Miller, P. A. Fedders, and D. I. Bolef, Acoustic Paramagnetic Resonance in a Dense Magnetic Insulator, Phys. Rev. Lett. **27**, 1063 (1971).

[24] F. S. Ham, Acoustic paramagnetic resonance spectrum of Cr^{2+} in MgO, Phys. Rev. B **4**, 3854 (1971).

[25] A. Hernández-Mínguez, A. V. Poshakinskiy, M. Hollenbach, P. V. Santos, and G. V. Astakhov, Acoustically induced coherent spin trapping, Sci. Adv. **7**, eabj5030 (2021).

[26] S. Maity, L. Shao, S. Bogdanović, S. Meesala, Y.-I. Sohn, N. Sinclair, B. Pingault, M. Chalupnik, C. Chia, L. Zheng, K. Lai, and M. Lončar, Coherent acoustic control of a single silicon vacancy spin in diamond, Nat. Commun. **11**, 1 (2020).

[27] E. R. MacQuarrie, T. A. Gosavi, N. R. Jungwirth, S. A. Bhave, and G. D. Fuchs, Mechanical Spin Control of Nitrogen-Vacancy Centers in Diamond, Phys. Rev. Lett. **111**, 227602 (2013).

[28] D. A. Golter, T. Oo, M. Amezcua, K. A. Stewart, and H. Wang, Optomechanical Quantum Control of a Nitrogen-Vacancy Center in Diamond, Phys. Rev. Lett. **116**, 143602 (2016).

[29] R. Jansen, P. Dhagat, A. Spiesser, H. Saito, and S. Yuasa, Analysis of surface acoustic wave induced spin resonance of a spin accumulation, Phys. Rev. B **101**, 214438 (2020).

[30] Y. Long, D. Zhang, C. Yang, J. Ge, H. Chen, and J. Ren, Realization of acoustic spin transport in metasurface waveguides, Nat. Commun. **11**, 1 (2020).

[31] T. Kawada, M. Kawaguchi, T. Funato, H. Kohno, and M. Hayashi, Acoustic spin Hall effect in strong spin-orbit metals, Sci. Adv. **7**, eabd9697 (2021).

[32] P. Bhalla, G. Vignale, and H. Rostami, Pseudogauge field driven acoustoelectric current in two-dimensional hexagonal Dirac materials, Phys. Rev. B **105**, 125407 (2022).

[33] R. Fandan, J. Pedrós, and F. Calle, Exciton–plasmon coupling in 2D semiconductors accessed by surface acoustic waves, ACS Photon. **8**, 1698 (2021).

[34] D. Scolfaro, M. Finamor, L. O. Trinchao, B. L. Rosa, A. Chaves, P. V. Santos, F. Iikawa, and O. D. Couto, Jr., Acoustically driven stark effect in transition metal dichalcogenide monolayers, ACS Nano **15**, 15371 (2021).

[35] P. Zhao, C. H. Sharma, R. Liang, C. Glasenapp, L. Mourokh, V. M. Kovalev, P. Huber, M. Prada, L. Tiemann, and R. H. Blick, Acoustically Induced Giant Synthetic Hall Voltages in Graphene, Phys. Rev. Lett. **128**, 256601 (2022).

[36] A. Hernández-Mínguez, Y.-T. Liou, and P. V. Santos, Interaction of surface acoustic waves with electronic excitations in graphene, J. Phys. D **51**, 383001 (2018).

[37] A. Politano, A. R. Marino, V. Formoso, D. Farías, R. Miranda, and G. Chiarello, Evidence for acoustic-like plasmons on epitaxial graphene on Pt(111), Phys. Rev. B **84**, 033401 (2011).

[38] I. G. Savenko, A. V. Kalameitsev, L. G. Mourokh, and V. M. Kovalev, Acoustomagnetoelectric effect in two-dimensional materials: Geometric resonances and Weiss oscillations, Phys. Rev. B **102**, 045407 (2020).

[39] S. Zheng, E. Wu, Z. Feng, R. Zhang, Y. Xie, Y. Yu, R. Zhang, Q. Li, J. Liu, W. Pang, H. Zhang, and D. Zhang, Acoustically

enhanced photodetection by a black phosphorus MoS_2 van der Waals heterojunction pn diode, Nanoscale **10**, 10148 (2018).

[40] S. Zheng, E. Wu, and H. Zhang, Anomalous acoustoelectric currents in few-layer black phosphorus nanocrystals, IEEE Trans. Nanotechnol. **17**, 590 (2018).

[41] S. Hoshino, R. Wakatsuki, K. Hamamoto, and N. Nagaosa, Nonreciprocal charge transport in two-dimensional noncentrosymmetric superconductors, Phys. Rev. B **98**, 054510 (2018).

[42] R. Oiwa, Y. Yanagi, and H. Kusunose, Time-reversal symmetry breaking superconductivity in hole-doped monolayer MoS_2, J. Phys. Soc. Jpn. **88**, 063703 (2019).

[43] Y. Ominato, J. Fujimoto, and M. Matsuo, Valley-Dependent Spin Transport in Monolayer Transition-Metal Dichalcogenides, Phys. Rev. Lett. **124**, 166803 (2020).

[44] E. A. Peterson, J. B. Haber, and J. B. Neaton, Superexchange-induced valley splitting in two-dimensional transition metal dichalcogenides: A first-principles study for rational design, Phys. Rev. B **104**, 205421 (2021).

[45] H. Ochoa and R. Roldán, Spin-orbit-mediated spin relaxation in monolayer MoS_2, Phys. Rev. B **87**, 245421 (2013).

[46] M. V. Boev and V. M. Kovalev, Rayleigh surface wave interaction with the 2D exciton Bose-Einstein condensate, J. Exp. Theor. Phys. **120**, 998 (2015).

[47] L. Landau, E. Lifšic, E. Lifshitz, A. Kosevich, J. Sykes, L. Pitaevskii, and W. Reid, in *Theory of Elasticity*, Course of Theoretical Physics Vol. 7 (Elsevier Science, New York, 1986).

[48] A. J. Pearce, E. Mariani, and G. Burkard, Tight-binding approach to strain and curvature in monolayer transition-metal dichalcogenides, Phys. Rev. B **94**, 155416 (2016).

[49] M. V. Durnev and S. A. Tarasenko, High-frequency nonlinear transport and photogalvanic effects in 2D topological insulators, Ann. Phys. **531**, 1800418 (2019).

[50] See Supplemental Material at http://link.aps.org/supplemental/10.1103/PhysRevB.106.155426 for calculations of analytical results.

[51] D. Costanzo, S. Jo, H. Berger, and A. F. Morpurgo, Gate-induced superconductivity in atomically thin MoS_2 crystals, Nat. Nanotechnol. **11**, 339 (2016).

[52] M. Siao, W. Shen, R. Chen, Z. Chang, M. Shih, Y. Chiu, and C.-M. Cheng, Two-dimensional electronic transport and surface electron accumulation in MoS_2, Nat. Commun. **9**, 1442 (2018).

[53] K. F. Mak, K. He, J. Shan, and T. F. Heinz, Control of valley polarization in monolayer MoS_2 by optical helicity, Nat. Nanotechnol. **7**, 494 (2012).